Transition to doubly diffusive chaos

Cédric Beaume
School of Mathematics, University of Leeds, Leeds LS2 9JT, United Kingdom

(Received 13 March 2020; accepted 15 September 2020; published 9 October 2020)

Doubly diffusive convection driven by horizontal gradients of temperature and salinity is studied in a three-dimensional enclosure of square horizontal cross section and large aspect ratio. Previous studies focused on the primary instability and revealed the formation of subcritical branches of spatially localized states. These states lose stability because of their twist instability, thereby precluding the presence of any related stable steady states beyond the primary bifurcation and giving rise to spontaneous temporal complexity for supercritical parameter values. This paper investigates the emergence of this behavior. In particular, chaos is shown to be produced at a crisis bifurcation located close to the primary bifurcation. The critical exponent related to this crisis bifurcation is computed and explains the unusually abrupt transition. The construction of a low-dimensional model highlights that only a few requirements are necessary for this type of transition to occur. As a consequence, it is believed to be observable in many other systems.

DOI: 10.1103/PhysRevFluids.5.103903

I. INTRODUCTION

Doubly diffusive convection, the convection of a fluid driven by density variations caused by two competing components, is a fascinating phenomenon that can lead to a wide range of behavior, some of which is still poorly understood. It has been mostly studied in oceanography, where it was shown to occur in 44% of the Earth's oceans [1]. In the oceanographic context, the flow is driven by temperature and salt variations and is usually referred to as thermohaline convection. It can lead to several instabilities, such as salt fingering, and is a major contributor to mixing currents [2–5]. Doubly diffusive convection is also studied in other contexts, such as in geology, where it is observed in magma chambers and at the Earth's core-mantle boundary [6,7], and in astrophysics [8–10].

In addition to the applied interest it draws, doubly diffusive convection is also a paradigm for pattern formation in fluids that has been studied in various configurations. The most studied such configuration is that of horizontal fluid layers placed within negative vertical gradients of temperature and salinity. Unlike Rayleigh–Bénard convection, this configuration yields primary bifurcations to standing and traveling waves that can be subcritical [11]. As a result, a wealth of time-dependent states has been observed both numerically [12–14] and experimentally [15–17], and temporal complexity, in the form of small amplitude dispersive chaos, emerges near criticality [18]. When the bifurcation to steady states is subcritical, secondary bifurcations have been found that lead to the formation of steady, spatially localized states known as *convectons* [19]. Their formation and their bifurcation diagram were characterized by Mercader *et al.* [20,21]: The convectons lie on a pair of branches undergoing well-bounded oscillations in parameter space in a behavior called *snaking*. Time-dependent localized states, in the form of traveling convection rolls within a spatially localized envelope traveling at a different speed, have also been observed to produce similar bifurcation diagrams [22] and the interplay between their stable and unstable manifolds has been elucidated by Watanabe *et al.* [23]. Symmetry-breaking perturbations, such as mixed boundary conditions for

the temperature [24] and slight inclinations of the fluid layer [25], were also found to imprint a nonzero traveling speed to the convectons.

The physical system of interest here is that of the doubly diffusive convection arising in a vertically extended, closed container driven by horizontal gradients of salinity and temperature. Here, unlike in the previously described configuration, the conduction state loses stability due to nonoscillatory modes, making steady-state dynamics of prime importance. Steady, spatially localized convection was once again found to be organized along two subcritical snaking branches. In two dimensions, some of these convectons are stable, and perturbing the forcing parameter (typically the Rayleigh number) outside the snaking region reveals a depinning instability in which the flow successively takes the form of localized states constituted of an increasing number of rolls until a stable, domain-filling state is reached [26]. Small-aspect-ratio, three-dimensional domains revealed secondary bifurcations along the branch of steady convection. These bifurcations produce tilted convection rolls and have a destabilizing effect on steady convection. Bergeon and Knobloch also observed a transition to chaos via a sequence of period-doubling bifurcations leading to a symmetric chaotic attractor that then undergoes an internal crisis to become asymmetric [27]. The three-dimensional convectons undergo a similar instability to that observed in small aspect-ratio domains: Pitchfork bifurcations can be found along the snaking branches that destabilize the convectons and give rise to a new family of (unstable) *twisted* convectons. The absence of any stable steady states drives the system to produce chaotic dynamics for supercritical parameter values [28]. The linear stability of the regular and twisted convectons revealed the emergence of transient temporal complexity in the subcritical regime but does not explain the sudden presence of chaos for parameter values near criticality [29].

The aim of this paper is to elucidate the transition to chaos observed in three-dimensional, doubly diffusive convection in a closed container extended in the vertical direction. The rest of this paper is structured as follows. The mathematical formalism of the problem is exposed in Sec. II, followed, in Sec. III, by the description of the successive instabilities leading from conduction to chaos. Section IV is devoted to the mechanism behind the observed transition to chaos. The paper continues with the construction of a phenomenological, low-dimensional model to highlight the generic character of the route to chaos identified in doubly diffusive convection. A short discussion concludes this paper.

II. PROBLEM SETUP

We consider the instability of a binary fluid mixture placed in a closed, three-dimensional container and subject to thermal and solutal gradients in the horizontal direction. The container has a square horizontal cross section and is extended in the vertical, x, direction with aspect ratio $L = 19.8536$, following earlier studies [28,29] and corresponding to eight critical wavelengths of the related two-dimensional problem [30]. The two vertical walls at constant z are maintained at fixed temperatures and salinities while the two other vertical walls are modeled using no-flux boundary conditions for both temperature and salt concentration. No-slip boundary conditions are used for the velocity at all the walls.

The fluid obeys the Navier–Stokes equation under the Boussinesq approximation, the incompressibility condition, the heat equation, and an advection-diffusion equation for the salinity. Upon nondimensionalization, these equations read

$$\mathrm{Pr}^{-1}[\partial_t \mathbf{u} + (\mathbf{u}\cdot\boldsymbol{\nabla})\mathbf{u}] = -\boldsymbol{\nabla} p + \mathrm{Ra}(T + NC)\mathbf{e_x} + \nabla^2\mathbf{u}, \tag{1}$$

$$\boldsymbol{\nabla}\cdot\mathbf{u} = 0, \tag{2}$$

$$\partial_t T + (\mathbf{u}\cdot\boldsymbol{\nabla})T = \nabla^2 T, \tag{3}$$

$$\partial_t C + (\mathbf{u}\cdot\boldsymbol{\nabla})C = \mathrm{Le}^{-1}\nabla^2 C, \tag{4}$$

where t is the time, $\mathbf{u}$ is the velocity field, p is the pressure, and $\mathbf{e_x}$ represents the vertical ascending unit vector. To write these equations, the temperature and salinity were rescaled in the following way:

$$T = \frac{T^* - T^*_{\text{ref}}}{\triangle T}, \qquad C = \frac{C^* - C^*_{\text{ref}}}{\triangle C}, \tag{5}$$

where T^* (resp. C^*) is the dimensional temperature (resp. salinity), T^*_{ref} (resp. C^*_{ref}) is the reference temperature (resp. salinity) taken at the $z = 0$ wall, and $\triangle T$ (resp. $\triangle C$) is the imposed temperature (resp. salinity) difference across the domain. System (1)–(4) is controlled by the following dimensionless numbers:

$$\text{Pr} = \frac{\nu}{\kappa}, \qquad \text{Ra} = \frac{g|\rho_T|\triangle T l^3}{\rho_0 \nu \kappa}, \qquad \text{Le} = \frac{\kappa}{D}, \qquad N = \frac{\rho_C \triangle C}{\rho_T \triangle T}, \tag{6}$$

where Pr is the Prandtl number, Ra is the Rayleigh number, Le is the Lewis number, N is the buoyancy ratio, ν is the kinematic viscosity of the fluid, κ is the thermal diffusivity of the fluid, g is the gravitational acceleration, ρ_T/ρ_0 is the thermal expansion coefficient in the Boussinesq approximation evaluated at the reference temperature, ρ_C/ρ_0 is the solutal expansion coefficient in the Boussinesq approximation evaluated at the reference salinity, ρ_0 is the fluid density at the reference temperature, l is the wall separation in both horizontal directions, and D is the molecular diffusivity of the fluid. The boundary conditions read

$$u = v = w = \partial_n T = \partial_n C = 0 \qquad \text{at } x = 0, L \text{ and } y = 0, 1, \tag{7}$$

$$u = v = w = T - z = C - z = 0 \qquad \text{at } z = 0, 1, \tag{8}$$

where u, v, and w are the projection of the velocity field $\mathbf{u}$ in the x, y, and z directions respectively, and where ∂_n represents the gradient in the direction normal to the wall.

We consider the case $N = -1$ so that the solutal and thermal contributions to the buoyancy compete with equal strength. This special case allows for the equations to admit the conductive solution $\mathbf{u} = \mathbf{0}$, $T = C = z$ and to be equivariant with respect to the dihedral group D_2 composed of the identity I and of the reflections

$$S_y : [u, v, w, \Theta, \Sigma](x, y, z) \to [u, -v, w, \Theta, \Sigma](x, 1 - y, z), \tag{9}$$

$$S_\triangle : [u, v, w, \Theta, \Sigma](x, y, z) \to -[u, -v, w, \Theta, \Sigma](L - x, y, 1 - z), \tag{10}$$

where $(\Theta, \Sigma) = (T - z, C - z)$ are the so-called convective variables. The composition of both the above reflections is the reflection with respect to the center point of the domain and is hereafter called S_c.

In the absence of dynamics in the y direction, the related two-dimensional system [26] only possesses the $S_\triangle$ symmetry (it is thus Z_2 equivariant, or $O(2)$ equivariant if spatially periodic boundary conditions are imposed in x). The instability from the conduction state is subcritical and the flow evolves toward a steady domain-filling state. In the three-dimensional system of interest here, the presence of the S_y symmetry is responsible for a major enrichment of the bifurcation diagram and of the observed dynamics, as described in the following sections for $\text{Le} = 11$ and $\text{Pr} = 1$.

III. INSTABILITY FROM THE CONDUCTIVE STATE

The conductive state ($u = v = w = 0$) is linearly stable until $\text{Ra} \approx 850.78$, where conduction develops as a result of two close bifurcations. The eigenmodes related to these two bifurcations produce arrays of steady convection rolls but are different in a subtle way, as shown in Figs. 1(a)

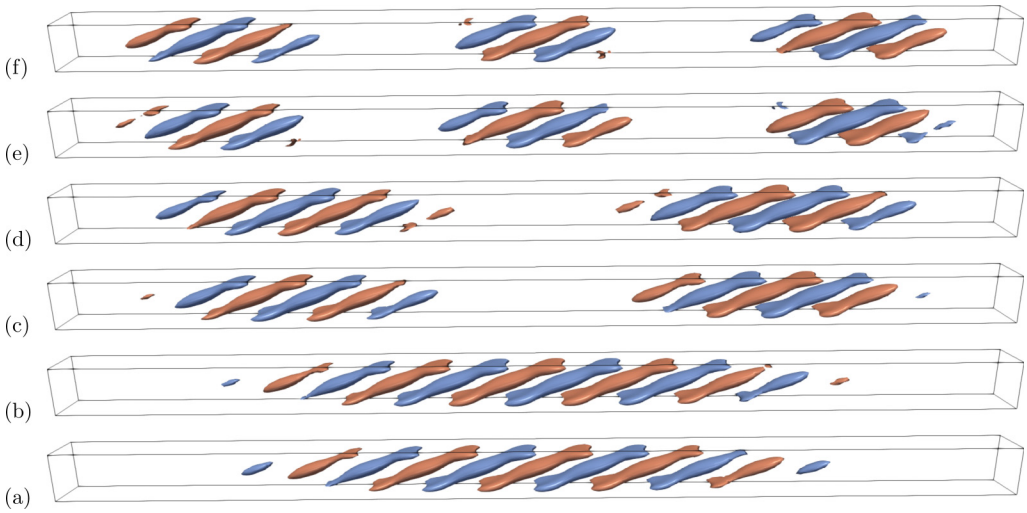

FIG. 1. Most unstable eigenmodes of the conductive state at Ra = 930 shown using two opposite contours of u. Eigenmode (a) is the first to become destabilizing at Ra $\approx$ 850.78. Eigenmode (b) is the one producing the subcritical patterns shown in Refs. [28,29] and becomes destabilizing at Ra $\approx$ 850.86. Eigenmodes (c) and (d) are two-pulse modes that are marginal at Ra $\approx$ 859, and eigemodes (e) and (f) are three-pulse modes marginal at Ra $\approx$ 872. In all figures, the gravity-bearing direction, x, is represented horizontally and the direction bearing the temperature and salinity gradients, z, is represented vertically.

and 1(b). On the one hand, the eigenmode in Fig. 1(b) satisfies all the symmetries of the system and creates a transcritical bifurcation at Ra $\approx$ 850.86, leading to the creation of a wide variety of localized states [28,29]. On the other hand, the eigenmode in Fig. 1(a) has a similar structure but with a phase shift of a quarter of the wavelength. As a result, it breaks both the $S_\triangle$ and the S_c symmetry (but preserves S_y). This eigenmode is responsible for the creation of a (subcritical) pitchfork bifurcation at Ra $\approx$ 850.78 [29]. The growth rates of the related instabilities are similar, e.g., $\lambda \approx 0.20$ at Ra = 930, where λ is the temporal growth rate and these eigenmodes remain the most unstable ones at all the values of the Rayleigh number tested. Other modes become destabilizing at higher values of the Rayleigh number: Bifurcations to two-pulse states are found at Ra $\approx$ 859 and to three-pulse states at Ra $\approx$ 872. The eigenmodes related to these bifurcations are represented for Ra = 930 in Fig. 1. At this value of the Rayleigh number, the two-pulse eigenmodes have growth rate $\lambda \approx 0.18$ while $\lambda \approx 0.15$ for the three-pulse eigenmodes. Crucially, all these eigenmodes preserve the symmetry S_y and trigger the formation of rolls with rotation axis $\mathbf{e_y}$, i.e., with dominant velocities in x and z. Figure 2 shows the growth rate of the most unstable eigenmodes for $845 \leqslant \text{Ra} \leqslant 950$. The instability hierarchy remains the same in the parameter region investigated: The leading instability is always one related to one-pulse perturbations.

As the instability grows, for Ra > 850.78, the rolls displaying downflow close to the hot and saline wall become suppressed in favor of the other rolls, giving rise to convective structures composed of corotating rolls [31]. Owing to the presence of walls at $x = 0$ and $x = L$, the structure grows from the center of the domain via successive nucleation of convection rolls. The growth of the instability is exemplified for Ra = 880 in Fig. 3. A preliminary simulation was initialized by the conductive state so that the instability developed from numerical noise. As the flow reached a domain-integrated kinetic energy of about 10^{-4}, the state was stored to be used as the initial condition of another simulation, shown in Figs. 3(a) and 3(c). Another simulation, shown in Figs. 3(b) and 3(d), was initialized on the opposite side of the stable manifold of the conduction state by changing the sign of all the components of $\mathbf{u}$, as well as those of Θ and Σ. The results are

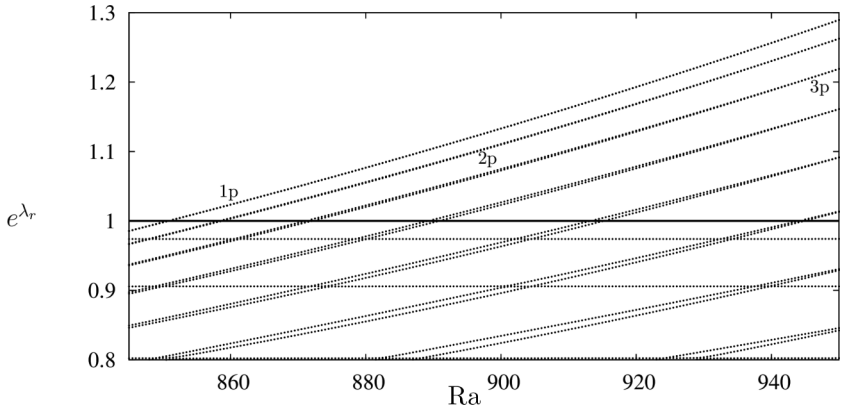

FIG. 2. Most unstable eigenvalues in the range $845 \leqslant \mathrm{Ra} \leqslant 950$ represented using the exponential of the real part of the eigenvalue $e^{\lambda_r} = e^{\mathrm{Re}(\lambda)}$. The thick line at $e^{\lambda_r} = 1$ represents marginality. The two eigenvalues representing the one-pulse eigenmodes are labeled 1p and are indistinguishable; so are those representing the two-pulse eigenmodes, labeled 2p, and those representing the three-pulse eigenmodes, labeled 3p.

shown through two flow indicators:

$$A_{\mathrm{conv}}(x,t) = \sqrt{\int_0^1 \int_0^1 u^2 dy\, dz}, \tag{11}$$

$$A_{\mathrm{tilt}}(x,t) = \sqrt{\int_0^1 \int_0^1 v^2 dy\, dz}, \tag{12}$$

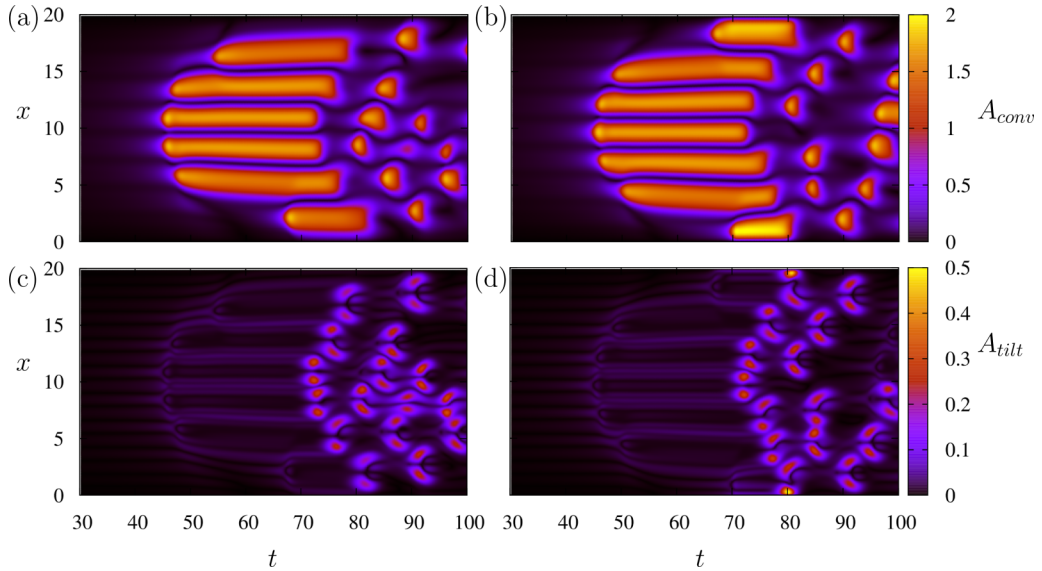

FIG. 3. Spatiotemporal growth of the convective pattern triggered by numerical noise at $\mathrm{Ra} = 880$ and represented by an indicator of the convection amplitude A_{conv} [see Eq. (11)] in panels (a) and (b) and by an indicator of the tilt amplitude A_{tilt} [see Eq. (12)] in panels (c) and (d) as a function of the time t and vertical coordinate x. The simulation in panels (a) and (c) and the one in panels (b) and (d) were initialized by small-amplitude states located on opposite side of the stable manifold of the conduction state.

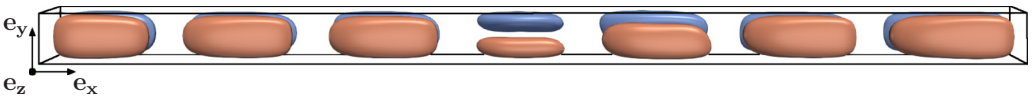

FIG. 4. Snapshot from the simulation in Figs. 3(b) and 3(d) taken at $t = 72.5$. The state is represented using contours $u = \pm 1$.

where $u = u(x, y, z, t)$ represents the velocity in the vertical, x, direction and $v = v(x, y, z, t)$ is the velocity component in the y direction. Indicator A_{conv} quantifies the convection amplitude owing to the fact that u typically represents the largest velocity component by nearly an order of magnitude. The rotation axis of the rolls emerging from the instability is $\mathbf{e_y}$ and, thus, their velocity has major components in the x and z directions. When a convection roll is impacted by the secondary instability, its axis tilts around $\mathbf{e_x}$, which generates a nonzero projection on $\mathbf{e_z}$ and results in non-negligible velocities in the y direction. Indicator A_{tilt} captures this flow feature: In the absence of tilt, $A_{\text{tilt}} \ll 1$. The first simulation, presented in Figs. 3(a) and 3(c), produces a structure consisting of four corotating rolls at $t = 50$ before the growth of a fifth one at $t \approx 55$ at the top of the structure, and of a sixth one at the bottom of the structure at $t \approx 67$, at which point convection is domain-filling. The other simulation, in Figs. 3(b) and 3(d), produces an array of five corotating rolls at $t = 50$ before two successive nucleations at $t \approx 67$ and $t \approx 70$, leading to a domain-filling seven-roll state before the emergence of temporal complexity. Owing to the magnitude difference between the growth rates of the one-pulse modes and the others for Rayleigh number values close to onset, any simulation initialized by a sufficiently small perturbation of the conductive state will lead to one or the other scenario described. At this stage, the flow is S_y symmetric and is reminiscent from spatially periodic convection [26]. Its roll count depends on the projection of the initial condition onto the unstable manifold of the conductive flow.

The domain-filling state formed through the process described above is unstable to a secondary instability that affects each roll individually. The axis of the affected rolls develops a nonzero component on $\mathbf{e_z}$ in addition to its dominant component on $\mathbf{e_y}$. An example of occurrence of this instability is shown in Fig. 4 by a state consisting of seven convection rolls. Most these rolls produce a flow rotating around $\mathbf{e_y}$, except for the central roll which is tilted and whose axis is no longer parallel to $\mathbf{e_y}$ but has now a non-negligible projection onto $\mathbf{e_z}$. Owing to the tilt, the high-velocity regions of the central roll are no longer parallel to the walls associated with the forcing boundary conditions. The roll can no longer be maintained and decays shortly after tilting, as shown in Fig. 3. The next rolls to be affected by the instability are the ones formed right after the central roll: The ones located next to it. The beginning of this second tilting event is visible in Fig. 4. Figure 3 shows that all the initial rolls survive for a duration of the order of 20 time units before tilting, decaying, and the emergence of chaotic dynamics characterized by shorter lived rolls.

To investigate the next stage of the dynamics, characterized by roll decay, a small amplitude state from the simulation shown in Figs. 3(b) and 3(d) is used to initialize a simulation in a domain constrained in such a way that only one roll is allowed to grow initially. The results are shown in Fig. 5 through the quantities A_{conv} and Φ_y, where

$$\Phi_y(x, t) = \int_0^1 \int_0^1 v dy\, dz. \tag{13}$$

The artificial damping slows down the growth of the instability: It now takes 260 units of time for the only roll to reach its full amplitude. The roll then survives for about 30 time units before its tilt becomes noticeable and reaches its maximum at $t \approx 292$, as shown by the y-flow rate profile in Figs. 5(b) and 6(a). The absence of a nearby wall and of any adjacent roll allows the localized roll to expand further than it normally would, as can be seen by comparing Fig. 6(a) with Fig. 3. As the roll tilts, its decay accelerates and it breaks from its center, forming two tilted rolls of smaller amplitude at $t \approx 293$ [see Fig. 6(b)] that continue to decay, albeit more slowly, until the flow energy

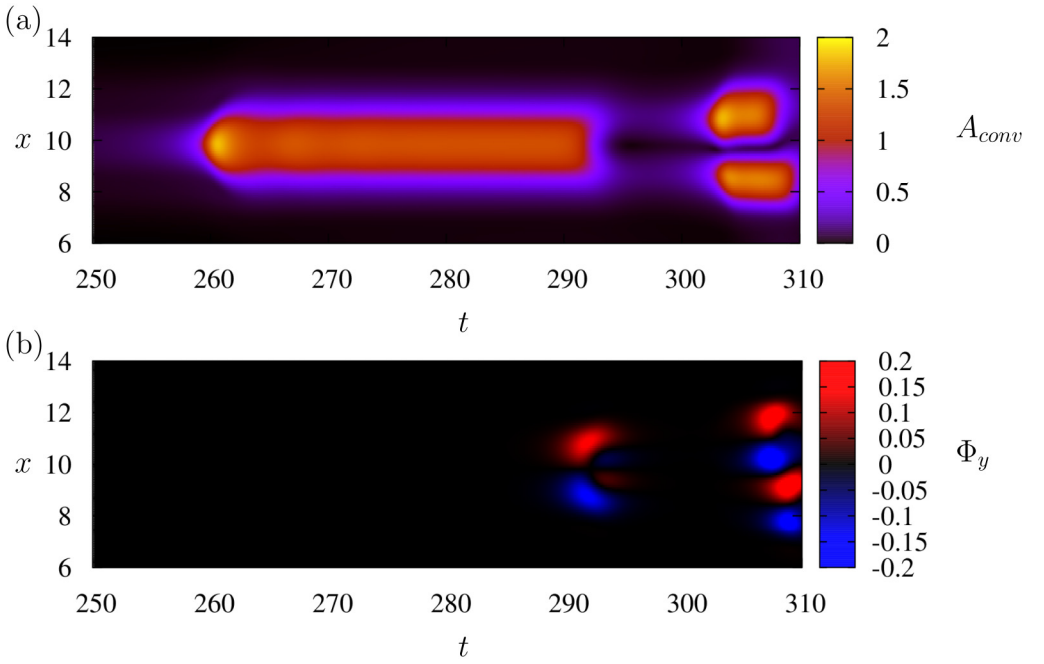

FIG. 5. Growth of the instability in a domain constrained by the addition of additional damping for $x < 7.4451$ and $x > 12.4085$. This simulation was initialized by the same initial condition used for the simulation shown in Figs. 3(b) and 3(d). The flow is represented in the central part of the domain through A_{conv} (a) quantifying the convection strength and the flow rate in the y direction Φ_y (b).

grows again at $t \approx 296$. The signature of these secondary rolls is also visible in the space-time plot in Fig. 5(b): As the red and blue patches indicating nonzero flow rate in the y direction move away from each other, two lower intensity patches of the opposite colors appear in between. In addition to highlighting the mechanisms by which the rolls decay, this provides insight into subsequent roll formation. The roll breaks up into two smaller structures carrying residual momentum. These two structures act like seeds for the later growth of the linear instability of the conduction state. In the above simulation, the two rolls that are produced at $t \approx 302$ are very close to the artificial edge of the domain and all subsequent dynamics are irrelevant. In a full domain simulation, interaction with the walls and other rolls leads to a strong partitioning of space: As the rolls rarely tilt (and subsequently decay) at the same time, there is generally not enough room for two rolls to form and the two seeds of energy quickly merge to yield only one new roll.

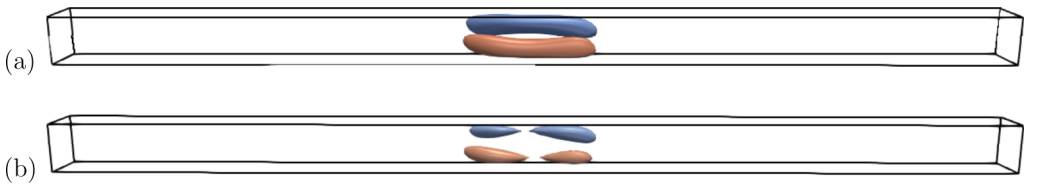

FIG. 6. Snapshots from the simulation shown in Fig. 5 taken at $t = 292$ (a) and $t = 293$ (b). The states are represented using contours $u = \pm 1$ (a) and $u = \pm 0.8$ (b). The orientation of the figure is similar to that of Fig. 4.

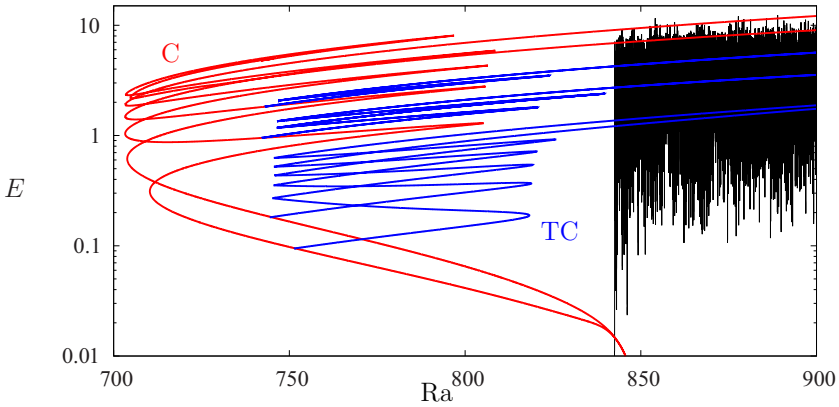

FIG. 7. Bifurcation diagram showing the total kinetic energy E [see Eq. (14)] as a function of the Rayleigh number Ra. The diagram shows branches of steady states in color: (red) the convecton branches C correspond to the branches $L^{\pm}$ in Refs. [28,29]; (blue) the twisted convecton branches TC correspond to the branches $L^{\pm}_{1,2}$ in Ref. [29]. The black line shows the result of a numerical simulation initialized at $\mathrm{Ra} = 900$ with an arbitrary instantaneous state obtained from chaotic dynamics at $\mathrm{Ra} = 900$. The Rayleigh number in that simulation was progressively decreased: $\mathrm{Ra} = 900 - \xi t$ with $\xi = 1/500$.

IV. CRISIS BIFURCATION

The sudden jump in amplitude between the end states observed on either side of the primary bifurcation point is typical of subcritical systems such as two-dimensional doubly diffusive convection [26]. The fact that the configuration considered here is three-dimensional introduces the symmetry S_y and allows for a secondary, symmetry-breaking instability to take place and for the destabilization of steady states that would otherwise be dynamics attractors. To identify the region of existence of the chaotic behavior, an arbitrary instantaneous flow state obtained from the chaotic dynamics at $\mathrm{Ra} = 900$ was selected as an initial condition for a simulation in which the Rayleigh number was progressively decreased. Figure 7 shows the result of this simulation superimposed onto the bifurcation diagram of the known steady states. The steady states bifurcate subcritically from the conductive state at $\mathrm{Ra} \approx 850.86$ and take the form of two pairs of intertwined branches of convectons C which produce snaking between $\mathrm{Ra} \approx 700$ and $\mathrm{Ra} \approx 810$ before going to larger Rayleigh numbers. They are subject to secondary bifurcations producing a family of secondary branches of twisted convectons TC, who undergo snaking between $\mathrm{Ra} \approx 740$ and $\mathrm{Ra} \approx 820$ before extending to large Rayleigh numbers. Several simulations were tested in which the Rayleigh number was a decreasing function of time. The rate of decrease of Ra in the simulation represented in Fig. 7 is $\xi = 1/500$. The flow initially displays large-amplitude oscillations spanning two orders of magnitude in the total kinetic energy,

$$E = \frac{1}{2}\int_0^1\int_0^1\int_0^L (u^2 + v^2 + w^2)\,dx\,dy\,dz, \tag{14}$$

and reaching values up to those of the most energetic convectons. This behavior persists down to $\mathrm{Ra} \approx 850$, where the flow tends to approach the conductive state more closely before its final decay at $\mathrm{Ra} \approx 842$. Analyzing other simulations revealed that slowing down the rate of decay of the Rayleigh number, i.e., lowering ξ, led to decay at larger values of the Rayleigh number but no simulation has been found to decay for $\mathrm{Ra} > 850$.

The sudden decay of chaotic dynamics observed in the simulation shown in Fig. 7 is typical of a crisis bifurcation. To characterize this transition, we look for the timescale over which chaos persists beyond the crisis, i.e., for $\mathrm{Ra} < \mathrm{Ra}_X$, where Ra_X is the crisis location to be determined. As the flow is highly dependent on the initial condition, we resort to the statistical analysis of a large number

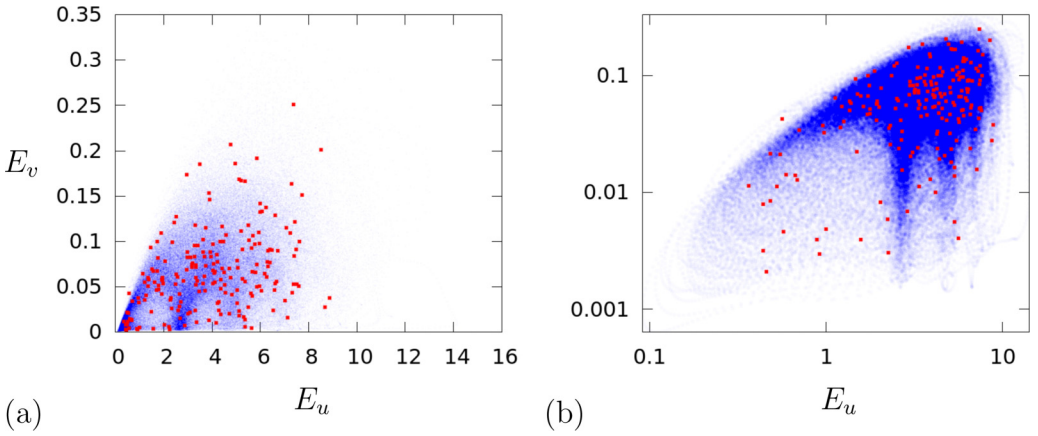

FIG. 8. Phase portraits of the flow obtained for a simulation at $Ra = 900$ represented by the reduced kinetic energies E_u and E_v defined in equations (15) and (16) in (a) linear and (b) logarithmic scales. The darker the blue, the more often the area is visited by the flow. The red squares indicate the 200 random selected flow states to serve as initial conditions for the statistical analysis of the crisis time-scales.

of simulations [32–34]. We select initial conditions randomly from a chaotic flow at Ra = 900. The latter simulation is represented via density plots for the reduced kinetic energies,

$$E_u = \frac{1}{2}\int_0^1\int_0^1\int_0^L u^2\,dx\,dy\,dz = \frac{1}{2}\int_0^L A_{\text{conv}}^2\,dx, \tag{15}$$

$$E_v = \frac{1}{2}\int_0^1\int_0^1\int_0^L v^2\,dx\,dy\,dz = \frac{1}{2}\int_0^L A_{\text{tilt}}^2\,dx, \tag{16}$$

in Fig. 8.

The chaotic flow is attracted by a region of phase space with fuzzy boundaries. To ensure fair sampling of the dynamics, we collect instantaneous flow states at large enough time intervals so that they satisfactorily represent the attractor: The selected flow states cover the whole area occupied by the attractor and their density is higher in areas that are more often visited, as shown in Fig. 8.

Simulations were initialized by the flow states identified in Fig. 8 for a number of subcritical Rayleigh numbers, ranging from Ra = 750, i.e., far away from the crisis, to Ra = 845, i.e., close to the crisis. The time at which the chaotic transient decayed or survival time, t_{decay}, was recorded by identifying the moment at which the total kinetic energy fell below $E < 10^{-3}$ for the first time. The distribution of survival times for a given value of Ra is statistical, as shown in Fig. 9(a). All the simulations decayed back to the conduction state in finite time and the associated timescale increased as the value of the Rayleigh number approached that of the crisis.

Much insight can be gained from basic dynamical considerations. First of all, the simulations have three stages: (i) an initial transient where the initial condition taken at Ra = 900 travels toward the displaced chaotic saddle, (ii) a chaotic transient where the flow is trapped in the saddle, and (iii) decay. The stage of interest here is the second one: The first stage is an artifact of the changed value of Ra and the third stage is dictated by the linear stability of the conduction state. It helps to think of the chaotic saddle as a topological ball with a hole. Once inside the ball, the trajectory bounces against its walls until it "finds" the hole, at which point the simulation enters its decay stage. This probabilistic depiction of chaotic saddles has led them to be called leaky attractors in the context of the transition to turbulence [35,36]. In this framework, the crisis bifurcation corresponds to the opening of the hole in the ball and the event corresponding to the trajectory exiting the chaotic saddle can be assimilated to a memoryless Poisson process. Given the above insight, we can infer that the probability of the trajectory exiting the leaky attractor follows an exponential distribution

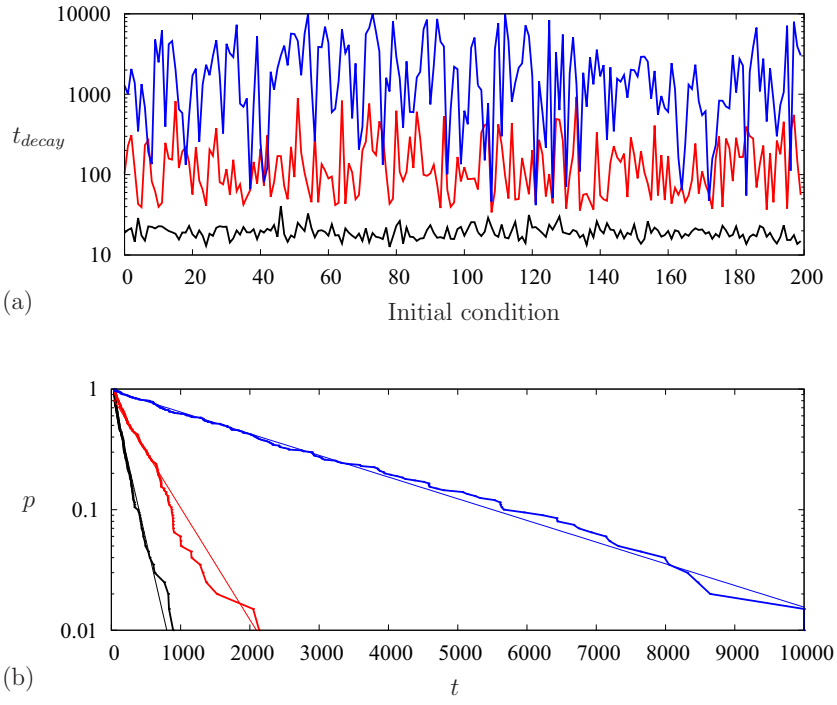

FIG. 9. (a) Time t_{decay} at which the simulation first reached values of the total kinetic energy $E < 10^{-3}$ as a function of the initial condition used for (black) Ra = 790, (red) Ra = 834, and (blue) Ra = 844. (b) Survival probability associated with similar data sets as in panel (a) but for (black) Ra = 834, (red) Ra = 838, and (blue) Ra = 844. The straight lines represent a fit to law (17) with $t_0 \approx -2.982$ and $t_c \approx 174.399$ for Ra = 834, $t_0 \approx -60.066$ and $t_c \approx 467.821$ for Ra = 838, and $t_0 \approx -58.300$ and $t_c \approx 2415.18$ for Ra = 844.

function of time and thus that the probability of a simulation not decaying before time t follows its complementary cumulative distribution function,

$$p(t) = e^{-\frac{t - t_0}{t_c}}, \tag{17}$$

where t_0 corresponds to the initial transient duration and t_c is the characteristic time associated with the process, both of which are functions of Ra. Similar survival analyses have been used to characterize transient turbulent flows [37,38] and more generally the spatiotemporal chaos generated by the complex Ginzburg–Landau equation [32]. Figure 9(b) shows the survival probability p for three sets of simulations taken at Ra = 834, Ra = 838, and Ra = 844 together with the corresponding least square fit to law (17). The data obtained through the flow simulations are well approximated by the exponential distribution, with the only visible departures from the law being observed in the tail of the distributions. This confirms the relevance of the chosen probabilistic approach. Further examination reveals that t_c increases with Ra, leading to longer simulations as we approach the crisis. The last complete set of simulations was obtained for Ra = 845. All the 200 initial conditions decayed to the conduction state, with the slowest ones staying in the vicinity of the chaotic saddle for more than 10^5 time units. The timescales involved in simulating the flow are such that it was computationally too expensive to pursue the numerical effort beyond Ra = 845.

The characteristic survival times t_c are shown as a function of the Rayleigh number in Fig. 10. Since the flow eventually decays down to the conduction state for subcritical values of Ra and that this state loses stability at Ra $\approx$ 850.78, it is logical to assume that the characteristic time associated

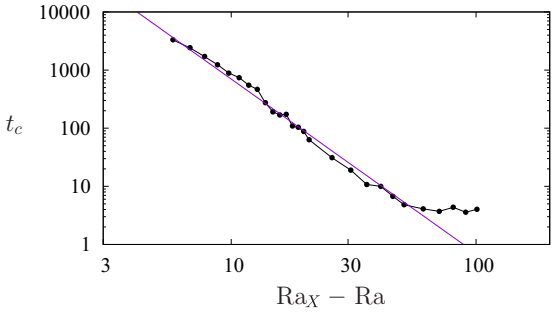

FIG. 10. Characteristic survival time of the chaotic transients t_c as a function of the distance to criticality $\mathrm{Ra}_X - \mathrm{Ra}$, where $\mathrm{Ra}_X = 850.78$ is chosen to be the location of the primary bifurcation point. The black dotted line corresponds to the numerical data while the straight line corresponds to the fit: $t_c \sim (\mathrm{Ra}_X - \mathrm{Ra})^{-3}$.

with the chaotic transient diverges for $\mathrm{Ra} \leqslant 850.78$. The results are therefore represented against the Rayleigh number offset by Ra_X, which is an approximate value for the crisis Rayleigh number. In practice, the data obtained do not allow the accurate determination of Ra_X, so $\mathrm{Ra}_X = 850.78$ was chosen. For $\mathrm{Ra}_X - \mathrm{Ra} < 50$, i.e., for $\mathrm{Ra} > 800$, t_c can be remarkably well approximated by

$$t_c \propto (\mathrm{Ra}_X - \mathrm{Ra})^{-\gamma}, \tag{18}$$

where $\gamma \approx 3$. This exponent is larger than the ones typically observed for crisis bifurcations in fluids. For example, Zammert and Eckhardt found two crises in plane Poiseuille flow, an interior crisis with $\gamma = 0.8$ and a boundary crisis with $\gamma = 1.5$ [33], and Kreilos *et al.* observed a boundary crisis in plane Couette flow with $\gamma = 2.1$ [36]. Figure 11 shows the evolution of the initial transient time t_0 as a function of the Rayleigh number. The initial transient lasts approximately 10 time units at $\mathrm{Ra} = 750$, the lowest Rayleigh number used, and grows monotonically until $\mathrm{Ra} = 825$, where it lasts approximately 27 time units. For values of the Rayleigh number beyond $\mathrm{Ra} = 825$, the results obtained are erratic and can take negative values. As the Rayleigh number is increased, the characteristic survival time grows at a much faster rate than the initial transient time. The latter becomes less important to the fitting function and more prone to statistical errors originating from the finite size of the sample. Figure 11(b) shows the initial transient time normalized by the characteristic survival time as a function of Ra and clearly shows that, in the region where t_0 is

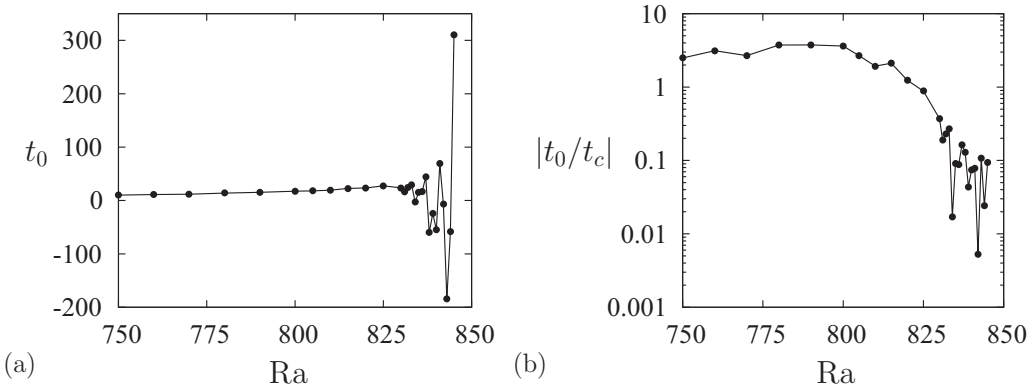

FIG. 11. (a) Initial transient time t_0 and (b) its absolute value normalized by the characteristic survival time t_c as a function of the Rayleigh number Ra.

poorly approximated (Ra $>$ 825), the absolute value of t_0 remains small compared to the values of t_c.

V. LOW-DIMENSIONAL TRANSITION MODEL

Close to the crisis bifurcation, the convection rolls seem to have a well-defined size and location in the physical domain. We can thus model the dynamics in the vicinity of the crisis by using a system of N_r coupled oscillators, each oscillator modeling one roll via two quantities: the convection energy, c, describing the energy contained in the x component of the velocity and main component of any convective flow observed; and the tilt, τ, describing the intensity of the y component of the velocity within that roll. The quantity c (resp. τ) can be thought of as the analog of A^2_{conv} (resp. Φ_y).

A. One-roll system

An essential feature of doubly diffusive convection (hereafter DDC) is the presence of subcritical untilted states, as shown by the branches labeled C in the bifurcation diagram in Fig. 7. A similar bifurcation diagram to that of such states can be obtained by setting a dynamical equation for c containing a simple quadratic-cubic nonlinearity and by simply damping out τ:

$$\partial_t c = rc + c^2 - c^3, \tag{19}$$

$$\partial_t \tau = -\gamma\tau, \tag{20}$$

where r is the forcing parameter, akin to the Rayleigh number, and $\gamma \geqslant 0$ is the tilt decay rate. In DDC, a destabilizing instability arises at a critical roll amplitude [28]. To model this, convection and tilt can be coupled in Eq. (20) such that when c is larger than a threshold value (function of γ), the untilted ($\tau = 0$) states become unstable. This coupled system writes

$$\partial_t c = rc + c^2 - c^3 - \beta c\tau^2, \tag{21}$$

$$\partial_t \tau = -\gamma\tau + \frac{\beta}{2}c\tau, \tag{22}$$

where $\beta \geqslant 0$ is the rate of energy transfer between the tilt energy τ^2 and the convection energy c. The effect of this coupling is to destabilize any solution $(c, \tau) = (c, 0)$ when $c > 2\gamma/\beta$ and, thus, to prevent the hysteresis by destabilizing the upper branch. The system presented above is similar to Eqs. (16) and (17) of Bergeon and Knobloch [27], except for the absence of one term that the authors deemed to have "[no] qualitative effect."

System (21) and (22) admits four steady states:

$$\text{Cond} : (c, \tau) = (0, 0), \tag{23}$$

$$\text{Lower} : (c, \tau) = \left(\frac{1}{2} - \frac{1}{2}\sqrt{1 + 4r}, 0\right), \tag{24}$$

$$\text{Upper} : (c, \tau) = \left(\frac{1}{2} + \frac{1}{2}\sqrt{1 + 4r}, 0\right), \tag{25}$$

$$\text{Twist} : (c, \tau) = \left(\frac{2\gamma}{\beta}, \pm\sqrt{\frac{r}{\beta} + \frac{2\gamma}{\beta^2} - \frac{4\gamma^2}{\beta^3}}\right), \tag{26}$$

where the subcritical state Lower bifurcates from the conduction state, Cond, at $r = 0$ and extends down to $r_s = -1/4$, where it undergoes a stabilizing saddle-node bifurcation producing the upper branch. The state Twist bifurcates from either Lower or Upper depending on the value of the group $2\gamma/\beta$. In DDC, this occurs when the roll energy is about 10% of the maximum roll energy within

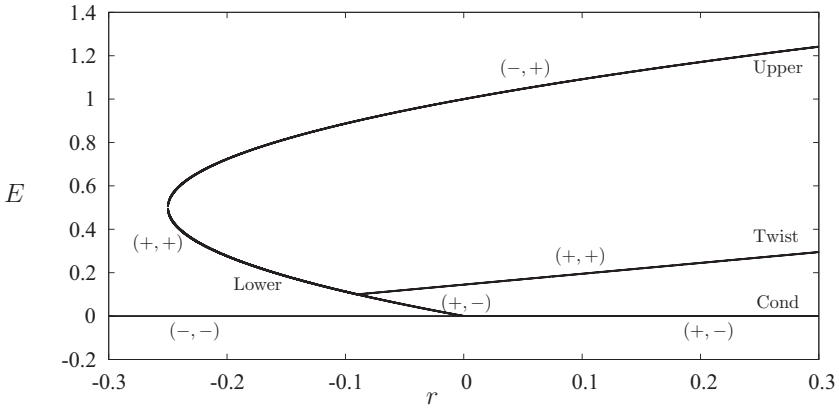

FIG. 12. Bifurcation diagram for systems (21) and (22) with $\beta = 2$ and $\gamma = 0.1$. The steady solutions are represented via the energy $E = c + \tau^2$ vs the reduced Rayleigh number r. The stability of each solution is shown in the following way: $(\mathrm{eig}_c, \mathrm{eig}_\tau)$, where eig_c (resp. eig_τ) represents the sign of the growth rate of the convection (resp. twist) eigenmode. Although the eigenmodes associated with the linear stability of Twist are not so trivial, they have, for simplicity, been represented in the same fashion.

the snaking region, implying that $2\gamma/\beta \approx 0.1$ and placing this bifurcation along the Lower branch. The resulting bifurcation diagram is shown for $\beta = 2$ and $\gamma = 0.1$ in Fig. 12.

The presence of the twist bifurcation alters the stability of the large amplitude steady states. The eigenmodes of the $\tau = 0$ states (Cond, Lower, and Upper) are decoupled and correspond either to pure convection or tilt. The former is responsible for the primary bifurcation at $r = 0$ and destabilizes Lower for $-1/4 < r < 0$, becoming stabilizing again at the saddle-node and creating a heteroclinic connection between Lower/Cond and Upper. Along the lower branch, the twist eigenmode becomes destabilizing at $r_\tau = 4\gamma^2/\beta^2 - 2\gamma/\beta = -0.09$, raising the dimension of the unstable manifold of both Lower for $r < r_\tau$ and Upper. The bifurcation at r_τ is the surrogate to the twist bifurcation in DDC and produces the solution Twist. The eigenmodes of Twist do not project trivially onto c or τ and both eigenvalues collide to form a pair of complex conjugate eigenvalues at $r_c = \delta^2(4\delta - 1)^2/(2\gamma) + 2\delta(2\delta - 1) = -0.082$, where $\delta = \gamma/\beta$.

For $r > 0$, no stable, $c \geqslant 0$ state exists and the dynamics takes the form of periodic orbits driven by the stable and unstable manifolds of the three fixed points. Three examples of such stable periodic orbits are shown in Fig. 13. Starting from an initial condition near Cond, the orbit follows the unstable manifold of Cond, which is also the stable manifold of Upper, as the convection amplitude grows. The orbit is subsequently repelled along the unstable (twist) manifold of Upper, which results in the increase of the twist energy, thereby suppressing convection and leading to the closure of the orbit as it approaches the stable manifold of Cond. This oscillatory behavior is further supported by the oscillatory instability of Twist. The orbits shown in Fig. 13 approach Cond and Upper as r is decreased; however, they are not formed at a global bifurcation at $r = 0$ but at a heteroclinic bifurcation just below $r = 0$. This was predicted by Bergeon and Knobloch in Ref. [27]: The case at hand is similar to their Fig. 15(a) [39]. To illustrate this, Fig. 14 shows the bifurcation diagram with the periodic orbit for $\gamma = 0.25$, where the global bifurcation is at an appreciable distance away from $r = 0$. The periodic orbit collides with Lower and Upper at a heteroclinic bifurcation located at $r_{\mathrm{het}} \approx -0.01$. As a result, there exists an interval in r, albeit small, in which the system is bistable.

B. N_r-roll system

There are various ways to couple rolls together. Here, the point is not to be exhaustive but rather to show a simple example of coupling that can lead to chaos immediately above onset. In DDC,

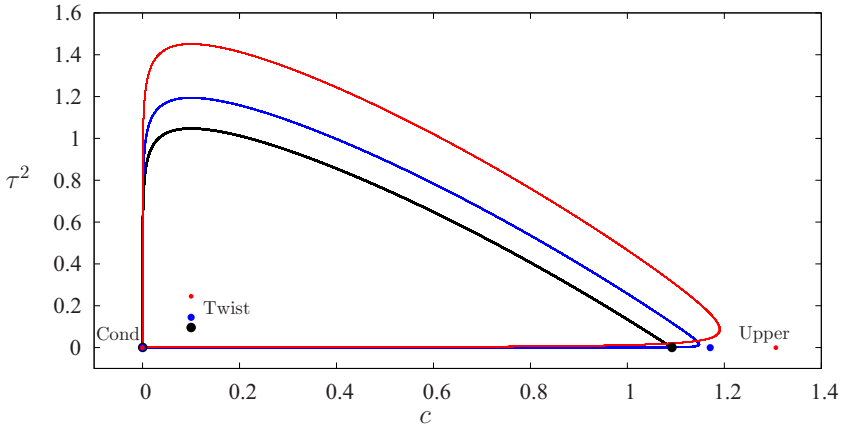

FIG. 13. Phase portrait showing the twist energy τ^2 as a function of the convection energy c for simulations at $r = 0.1$ (black), $r = 0.2$ (blue), and $r = 0.4$ (red). The three fixed points (Cond, Upper, and Twist) are shown using dots while the stable periodic orbits are shown in solid lines. Parameters are $\beta = 2$ and $\gamma = 0.1$.

as a roll tilts, its convection amplitude decays, vanishing from the center toward the outside and forming, for a very short period of time, two smaller tilted rolls (see Figs. 5 and 6). Following the decay of these rolls, two seeds of kinetic energy are left behind that may lead to the growth of two rolls instead of one at the newly vacated location. The following coupled system takes inspiration from this observation:

$$\partial_t c_i = r c_i + c_i^2 - c_i^3 - \beta c_i \tau_i^2 + \eta\left(\tau_{i-1}^2 + \tau_{i+1}^2\right), \tag{27}$$

$$\partial_t \tau_i = -\gamma \tau_i + \frac{\beta}{2} c_i \tau_i - \eta \tau_i, \tag{28}$$

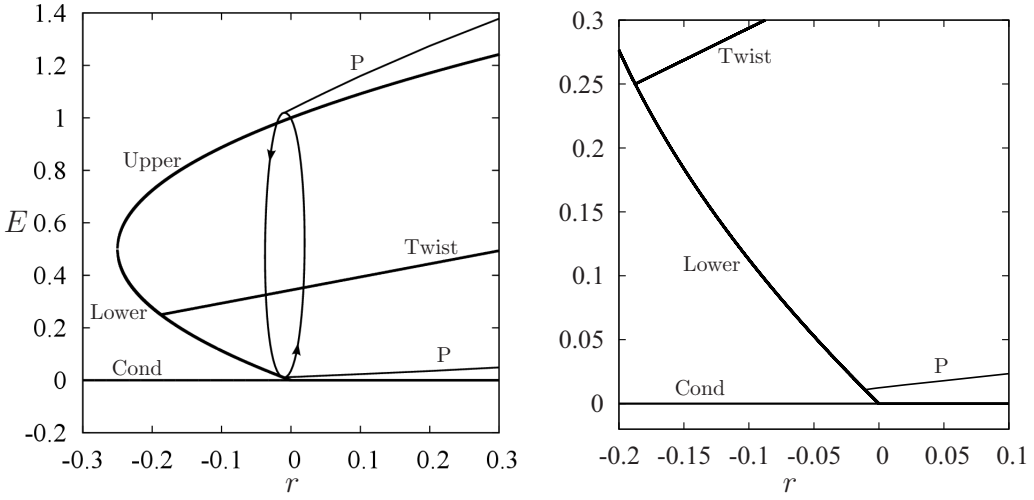

FIG. 14. Bifurcation diagram showing the periodic orbit P on top of the steady states represented using the extrema values of E as a function of r for $\beta = 2$ and $\gamma = 0.25$. The right panel is an enlargement of the left panel to show the bifurcation to periodic orbits.

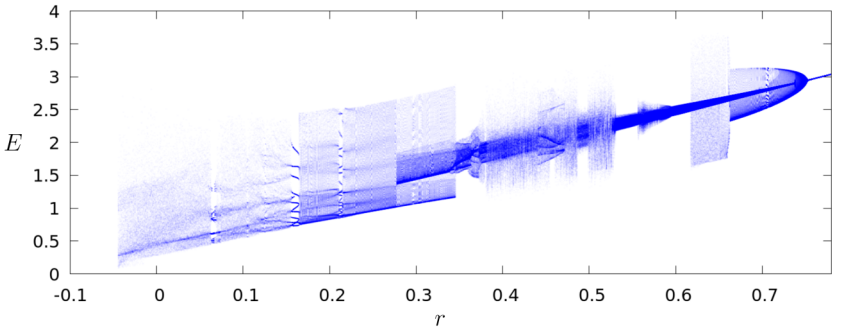

FIG. 15. Bifurcation diagram showing the value of the energy E as a function of r for system (27) and (28) with six rolls, $\beta = 2$, $\gamma = 0.1$ and $\eta = 0.01$. The points reported are Poincaré section intersects where the Poincaré plane is defined via the conditions $\partial_t E = 0$ and $\partial_t^2 E > 0$. The diagram shows the density of Poincaré intersects: the more opaque, the denser.

where the subscript i indicates the ith roll, $i = 1, ..., N_r$, and $\eta \geqslant 0$. The coupling term converts some of the tilt energy of the ith roll into convection energy for the adjacent rolls. More specifically, the term $-\eta\tau_i$ in Eq. (28) removes tilt energy at rate $-2\eta\tau_i^2$, half of which is reinjected in Eq. (27) for the $(i-1)$-th roll, the other half being reinjected in the same equation but for the $(i+1)$-th roll.

No-slip boundary conditions can be modeled by assuming that the rolls at the extrema of the domain lose tilt energy at the same rate as central rolls but will only receive convection energy from one neighbor: $\tau_0 = 0$ and $\tau_{N_r+1} = 0$. To illustrate the complexity of the behavior obtained by weakly coupling the oscillators, we set $\beta = 2$, $\gamma = 0.1$, and $\eta = 0.01$, and consider the Poincaré section corresponding to the conditions

$$\frac{\partial E}{\partial t} = \frac{\partial(\bar{c} + \bar{\tau^2})}{\partial t} = 0 \qquad \text{and} \qquad \frac{\partial^2 E}{\partial t^2} > 0, \tag{29}$$

where

$$\bar{c} = \Sigma_{i=1}^{N_r} c_i, \qquad \bar{\tau^2} = \Sigma_{i=1}^{N_r} \tau_i^2. \tag{30}$$

Intersections of the trajectory with this Poincaré section correspond to local minima of the total energy of the system. Figure 15 shows the resulting diagram for system (27) and (28) with six rolls. An initial run consisted in a series of simulations, the first of which was set at $r = -0.1$ and the last of which at $r = 0.8$ with increments $\triangle r = 5 \times 10^{-4}$. The first simulation was initialized using a random initial condition of small amplitude, and then each successive simulation was initialized by the last state of the simulation that preceded it. Although the simulations were run for 15 000 time units, only the Poincaré intersections occurring during the last 5000 time units were stored to avoid capturing any transient dynamics. A second run was then carried out in the reverse direction down to $r = -0.1$ to identify the subcritical extent of the chaotic region. Although the initial run identified the presence of an immediate transition to temporal complexity at $r = 0$, the second run revealed that this chaotic behavior persists down to $r \approx -0.044$, indicating a small region of coexistence between chaos and Cond. Figure 15 also indicates a number of distinct regions exhibiting qualitatively different dynamics. Some of these regions are chaotic, as indicated by a diffuse set of Poincaré intersects, while others are dominated by periodic orbits and only feature Poincaré intersects at well-defined values of the energy E. To illustrate these different dynamics, several simulations are reported in Fig. 16. The observed chaotic trajectory at $r = 0$ [Fig. 16(a)] displays little structure besides the dominating anticlockwise cycle resulting from the dynamics imposed by the uncoupled system (see Fig. 13). When $r < r_{\text{het}}$ in the uncoupled system, decay is unavoidable. On the other hand, in the presence of coupling, a neighboring roll with nonzero tilt energy provides a source of convection energy capable of restarting a decaying roll. This, in turn, makes it possible to observe

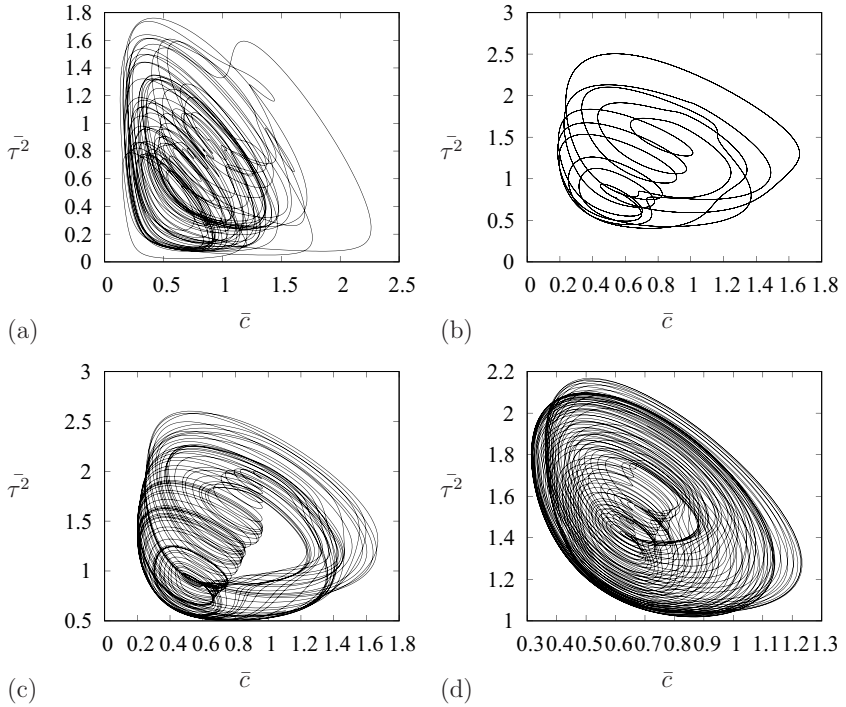

FIG. 16. Phase space trajectories represented onto the $\bar{c}$-$\bar{\tau}^2$ plane for (a) $r = 0$, (b) $r = 0.16$, (c) $r = 0.2$, and (d) $r = 0.3$. Each of these trajectories represents the evolution of the system over 1000 time units after an initial transient of suitable duration was discarded. Parameters are $N_r = 6$, $\beta = 2$, $\gamma = 0.1$, and $\eta = 0.01$.

nontrivial dynamics below r_{het}. As r is increased, the temporal dynamics simplifies and, by $r = 0.2$ [Fig. 13(c)], the trajectory follows two distinct stages. During the first stage, from the lowest energy point in the cycle to the point of maximum tilt energy $\bar{\tau}^2$, the system follows straightforward dynamics: The convection energy $\bar{c}$ first increases, leading to the buildup of tilt energy, which then suppresses convection. The second part of the cycle corresponds to the redistribution of twist energy into convection energy to neighboring rolls. As this happens, the trajectory spirals down to return to the point of minimal energy. This dynamical structure can be easily observed on the periodic orbit identified at $r = 0.16$ [Fig. 16(b)]. As the parameter is increased further, transitions to other attractors can be seen, such as the one occurring at $r \approx 0.28$ and leading to the dynamics shown in Fig. 16(d). This attractor is denser than the one shown in Fig. 16(c) and both coexist for a range of parameter values. Lastly, this temporal complexity terminates at $r \approx 0.75$ where the last (Hopf) bifurcation leads to the return to a simple periodic orbit.

VI. DISCUSSION

This paper dealt with doubly diffusive convection in a vertically extended domain with square horizontal cross section and forced by horizontal gradients of salinity and temperature. This flow configuration gives rise to a sudden transition to chaos that was here characterized via its successive temporal instabilities and as a dynamical systems process. While the linear instability from the conduction state produces an array of counter-rotating convection rolls, nonlinear effects select half of them, leading to an array of corotating rolls [31]. Past a certain convection amplitude, the convection rolls become unstable and tilt before decaying. This secondary instability initiates chaotic dynamics where shorter lived rolls are observed at well-defined locations in the physical

domain. These rolls obey similar dynamics to the one previously described: Owing to the instability of the conduction state, they evolve through cycles where they grow, tilt, and then decay. Weak interactions between these rolls seem to be responsible for temporal complexity by nontrivially modifying the duration of each of the cycle stage. This chaotic regime disappears at a crisis bifurcation located in the vicinity of the primary bifurcation. It was found that the crisis bifurcation is abrupt, with a critical exponent of about 3. To illustrate the dynamical phenomenon at play, a low-dimensional model was constructed based on basic observations of the bifurcation structure found in doubly diffusive convection. The model takes advantage of the fact that the convection rolls always occupy the same position and do not drift, so that they can be represented by oscillators. The equations for adjacent oscillators were coupled via the addition of terms inspired by the way rolls interact in doubly diffusive convection. The resulting phenomenological model exhibits a global bifurcation where time-dependent, long-lasting behavior arises at slightly subcritical values of the parameter which hints at the possible existence of a small region of bistability between the conductive state and chaos.

This paper elucidates the transition to chaos observed in doubly diffusive convection in Refs. [28,29]. While the aforementioned references focused on subcritical pattern formation, the transition to complex dynamics immediately at onset remained unclear. This paper shows that this transition to chaos is the result of a crisis bifurcation. Although crises are common in classical fluid dynamics [33,38,40,41], to the author's knowledge, it is observed here for the first time in the vicinity of the primary instability. The phenomenon identified here requires few conditions to take place, as shown by the construction of a low-dimensional, phenomenological model. It is further expected that any system displaying subcritical localized states subject to a secondary subcritical instability might display such an abrupt transition to chaos. This is the case in a variety of systems related to fluids which display spatially localized pattern formation: With few exceptions, they are subcritical and their high dimensionality makes the emergence of secondary instabilities likely. As such, this work may be of relevance to a large range of fluid systems.

ACKNOWLEDGMENTS

C.B. acknowledges A. Archer, E. Knobloch, P. Matthews, A. Pershin, and A. Rucklidge for fruitful discussions. Direct numerical simulations were undertaken on ARC3 and ARC4, part of the High Performance Computing facilities at the University of Leeds, UK.

[1] Y. You, A global ocean climatological atlas of the Turner angle: Implications for double-diffusion and water-mass structure, Deep Sea Res. **49**, 2075 (2002).
[2] A. J. Williams, Salt fingers observed in the Mediterranean outflow, Science **185**, 941 (1974).
[3] H. E. Huppert and J. S. Turner, Double-diffusive convection, J. Fluid Mech. **106**, 299 (1981).
[4] R. W. Schmitt, Double diffusion in oceanography, Annu. Rev. Fluid Mech. **26**, 255 (1994).
[5] J. Marotzke and J. R. Scott, Convective mixing and the thermohaline circulation, J. Phys. Oceanogr. **29**, 2962 (1999).
[6] U. Hansen and D. A. Yuen, Nonlinear physics of double-diffusive convection in geological systems, Earth Sci. Rev. **29**, 385 (1990).
[7] T. Lay, J. Hernlund, and B. A. Buffett, Core-mantle boundary heat flow, Nat. Geosci. **1**, 25 (2008).
[8] E. A. Spiegel, Semiconvection, Astrophys. Space Phys. **1**, 57 (1969).
[9] E. A. Spiegel, Convection in stars II. Special effects, Annu. Rev. Astron. Astrophys. **10**, 261 (1972).
[10] E. Rosenblum, P. Garaud, A. Traxler, and S. Stellmach, Turbulent mixing and layer formation in double-diffusive convection: 3D numerical simulations and theory, Ap. J. **731**, 66 (2011).
[11] E. Knobloch, A. Deane, J. Toomre, and D. R. Moore, Doubly diffusive waves, Contemp. Math. **56**, 203 (1986).

[12] O. Batiste, E. Knobloch, I. Mercader, and M. Net, Simulations of oscillatory binary fluid convection in large aspect ratio containers, Phys. Rev. E **65**, 016303 (2001).
[13] O. Batiste and E. Knobloch, Simulations of oscillatory convection in ^{3}He-^{4}He mixtures in moderate aspect ratio containers, Phys. Fluids **17**, 064102 (2005).
[14] O. Batiste and E. Knobloch, Simulations of Localized States of Stationary Convection in ^{3}He-^{4}He Mixtures, Phys. Rev. Lett. **95**, 244501 (2005).
[15] P. Kolodner, C. M. Surko, and H. Williams, Dynamics of traveling waves near the onset of convection in binary fluid mixtures, Phys. D (Amsterdam, Neth.) **37**, 319 (1989).
[16] P. Kolodner, Stable and unstable pulses of traveling-wave convection, Phys. Rev. A **43**, 2827 (1991).
[17] P. Kolodner, Repeated transients of weakly nonlinear traveling-wave convection, Phys. Rev. E **47**, 1038 (1993).
[18] O. Batiste, E. Knobloch, A. Alonso, and I. Mercader, Spatially localized binary-fluid convection, J. Fluid Mech. **560**, 149 (2006).
[19] C. Beaume, A. Bergeon, and E. Knobloch, Homoclinic snaking of localized states in doubly diffusive convection, Phys. Fluids **23**, 094102 (2011).
[20] I. Mercader, O. Batiste, A. Alonso, and E. Knobloch, Localized pinning states in closed containers: Homoclinic snaking without bistability, Phys. Rev. E **80**, 025201(R) (2009).
[21] I. Mercader, O. Batiste, A. Alonso, and E. Knobloch, Convectons, anticonvectons and multiconvectons in binary fluid convection, J. Fluid Mech. **667**, 586 (2011).
[22] T. Watanabe, M. Iima, and Y. Nishiura, Spontaneous formation of traveling localized structures and their asymptotic behavior in binary fluid convection, J. Fluid Mech. **712**, 219 (2012).
[23] T. Watanabe, M. Iima, and Y. Nishiura, A skeleton of collision dynamics: Hierarchical network structure among even-symmetric steady pulses in binary fluid convection, SIAM J. Appl. Dyn. Sys. **15**, 789 (2016).
[24] I. Mercader, O. Batiste, A. Alonso, and E. Knobloch, Travelling convectons in binary fluid convection, J. Fluid Mech. **722**, 240 (2013).
[25] I. Mercader, O. Batiste, A. Alonso, and E. Knobloch, Effect of small inclination on binary convection in elongated rectangular cells, Phys. Rev. E **99**, 023113 (2019).
[26] A. Bergeon and E. Knobloch, Spatially localized states in natural doubly diffusive convection, Phys. Fluids **20**, 034102 (2008).
[27] A. Bergeon and E. Knobloch, Natural doubly diffusive convection in three-dimensional enclosures, Phys. Fluids **14**, 3233 (2002).
[28] C. Beaume, A. Bergeon, and E. Knobloch, Convectons and secondary snaking in three-dimensional natural doubly diffusive convection, Phys. Fluids **25**, 024105 (2013).
[29] C. Beaume, A. Bergeon, and E. Knobloch, Three-dimensional doubly diffusive convectons: Instability and transition to complex dynamics, J. Fluid Mech. **840**, 74 (2018).
[30] S. Xin, P. Le Quéré, and L. S. Tuckerman, Bifurcation analysis of double-diffusive convection with opposing horizontal thermal and solutal gradients, Phys. Fluids **10**, 850 (1998).
[31] S. Thangam, A. Zebib, and C. F. Chen, Double-diffusive convection in an inclined fluid layer, J. Fluid Mech. **116**, 363 (1982).
[32] S. M. Houghton, E. Knobloch, S. M. Tobias, and M. R. E. Proctor, Transient spatio-temporal chaos in the complex Ginzburg–Landau equation on long domains, Phys. Lett. A **374**, 2030 (2010).
[33] S. Zammert and B. Eckhardt, Crisis bifurcation in plane Poiseuille flow, Phys. Rev. E **91**, 041003(R) (2015).
[34] P. Ritter, F. Mellibovsky, and M. Avila, Emergence of spatio-temporal dynamics from exact coherent solutions in pipe flow, New J. Phys. **18**, 083031 (2016).
[35] T. Kreilos and B. Eckhardt, Periodic orbits near onset of chaos in plane Couette flow, Chaos **22**, 047505 (2012).
[36] T. Kreilos, B. Eckhardt, and T. M. Schneider, Increasing Lifetimes and the Growing Saddles of Shear Flow Turbulence, Phys. Rev. Lett. **112**, 044503 (2014).
[37] B. Hof, J. Westerweel, T. M. Schneider, and B. Eckhardt, Finite lifetime of turbulence in shear flows, Nature (London) **443**, 59 (2006).

[38] A. P. Willis and R. R. Kerswell, Critical Behavior in the Relaminarization of Localized Turbulence in Pipe Flow, Phys. Rev. Lett. **98**, 014501 (2007).

[39] Here, r (resp. γ) corresponds to their μ (resp. ν), and where their γ corresponds to the value of their μ at the global bifurcation that is always negative but very close to 0 for small ν.

[40] M. Avila, A. P. Willis, and B. Hof, On the transient nature of localized pipe flow turbulence, J. Fluid Mech. **646**, 127 (2010).

[41] L. Oteski, Y. Duguet, L. Pastur, and P. Le Quéré, Quasiperiodic routes to chaos in confined two-dimensional differential convection, Phys. Rev. E **92**, 043020 (2015).